First Tests of the Interferometer in the Micro-Arcsecond Metrology Testbed (MAM)

Andreas C. Kuhnert, Stuart B. Shaklan, Janice Shen, Andrew Carlson, L. Steven Azevedo

Jet Propulsion Laboratory, California Institute of Technology, Pasadena, CA 91109

ABSTRACT

The Space Interferometry Mission (SIM) relies on interferometry and metrology capable of measuring the change in the optical path difference with picometer accuracy. For the last two years we designed and built the Micro-Arcsecond Metrology (MAM) Testbed, the key technology demonstration for SIM. In a parallel effort the data analysis code was written. The interferometer was first used in a modified configuration: white light and light from a HeNe-laser was emerging from a fiber, collimated and split into the two arms with their respective delay lines. The recombined light was then dispersed onto the CCD camera. The tests done using this interferometer resulted in data on the effects that influence the accurate determination of the fringe phase delay: i) alignment effects; ii) CCD camera parameters; iii) path length stability, and iv) analysis related inaccuracies. While offsetting the interferometer from equal arm length, the OPD was dithered using PZT-actuated mirrors. The white-light fringe was captured for each step. At the same time the (HeNe) laser light was monitored with two photo detectors – one serving as an intensity monitor, the second one monitoring the interfered laser light. This technique was used to accurately measure the path length changes by analyzing the linear parts of the HeNe sinusoidal interference signal normalized by the HeNe intensity signal. This simple metrology system is designed to determine the optical path length changes to about 100 pm.

Keywords: Interferometry, Space Interferometry Mission, astrometry, picometer metrology.

1. INTRODUCTION

The Space Interferometry Mission (SIM) under development at the Jet Propulsion Laboratory is designed to perform high-precision astrometry of a large sample of galactic and extra-galactic objects. With its unprecedented 4 micro-arcsecond accuracy, SIM can detect thousands of extra-solar planets, measure the distance to the furthest stars in our galaxy, and calibrate cosmological distance beacons [1].

In parallel with the spacecraft and flight instrument design efforts, JPL is building several testbeds to develop the necessary technology required for a successful mission. This paper describes the initial tests performed with the interferometer in the Micro-Arcsecond Metrology (MAM) Testbed [2]. MAM is designed to demonstrate simultaneous high-precision laser metrology and white-light fringe measurements in a SIM-like interferometer.

This paper reports on the first phase of the planned measurements: using a commercially available CCD camera to capture the dispersed white-light fringe. In the second phase we will install a CCD camera that was developed by JPL and is currently under testing. As an interim step, we are currently testing a science-grade CCD developed by SciMeasure[4] based on the same CCD as the JPL camera. Additionally, we will install the final metrology system based on heterodyne interferometers [3].

2. INTERFEROMETER SETUP

The interferometer was installed in early fall 1999. However, it is not in its final stellar interferometer configuration; for the tests it is configured as a Michelson interferometer, as shown in Figure 1. It is installed on one of the optical benches in the MAM vacuum chamber.

The light from a halogen flashlight operated from a stabilized power supply is combined with the light from a HeNe laser and coupled into a single-mode fiber outside the vacuum chamber. This light emerges from the fiber inside the chamber and is collimated by a parabolic mirror, i.e. the "white-light" and the HeNe light trace a common optical path. The light is then split by three 50/50 beamsplitters. The first one directs light to a photo detector to monitor the white-light intensity out of the fiber, the second beamsplitter does the same for the HeNe light (with proper color glass filters in front of the photo detectors). The third beamsplitter, a metallic sandwich beamsplitter, splits the light into the two interferometer arms. The fringe/guide separator, an optic that is used to separate the angle-tracking light from the fringe light, then reflects the light towards the

delay line. A dichroic mirror on the first surface of a window reflects the light above 600 nm and passes the shorter wavelengths. The red light is used for fringes after being combined with the red light from the other arm. The blue light reflects from a mirror that is slightly tilted with respect to the first surface and is used to monitor angle changes of the light.

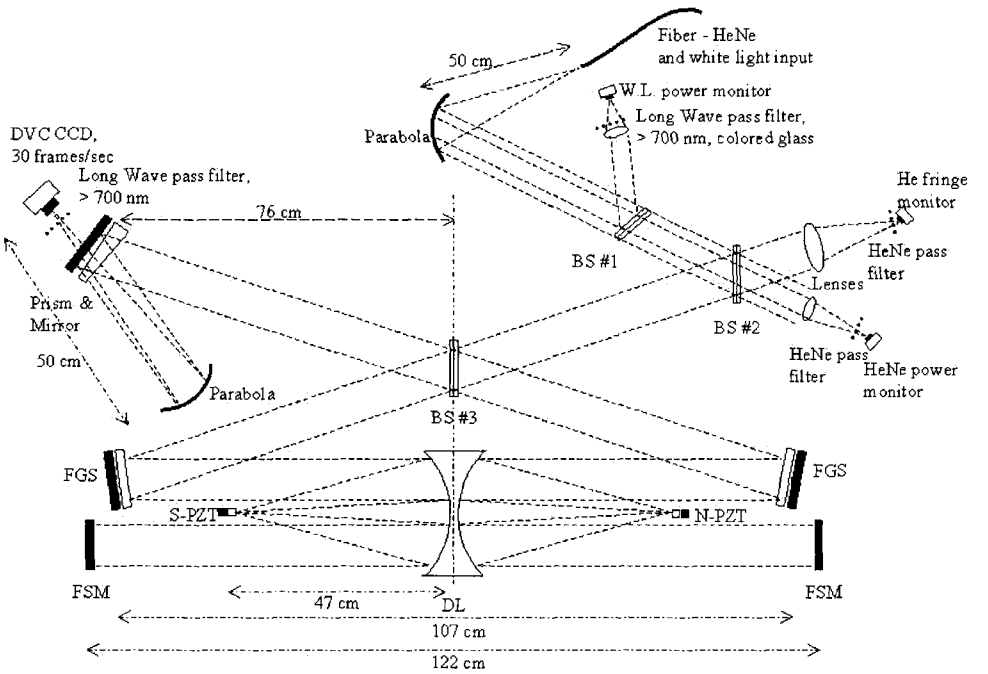

Figure 1 MAM interferometer in its present configuration. BS – 50/50 beamsplitter; W.L. – white-light; DL – delay line; FGS – fringe/guide separator; FSM – fast steering mirror; N-PZT & S-PZT – north & south piezo actuated secondary mirrors.

The delay line uses a dual parabola as the primary optical element in both beams. Motion of the delay line by a distance d causes an optical path difference between the arms of 8d. The delay line secondary mirrors are mounted on momentum compensated PZT actuators, motion of the secondary mirrors causes an optical path difference between the arms 4 times that motion.

The light is then reflected back by mirrors that are mounted on a piezo actuated tip-tilt stage (FSM). After combining the beams at beamsplitter #3, the red beams in the CCD arm are dispersed by a prism/mirror system. The double-pass fused-silica prism achieves a dispersion that is highly uniform in wave-number while directing the central wavelength to be roughly parallel to the blue guide light that reflected from its front surface. A parabola then focuses the beam onto the CCD camera. Fringes are seen in the dispersed spectrum together with adjacent guide spots. The HeNe light is combined at this beamsplitter as well and the path length dependant intensity is detected with a photo detector. We have not made use of the white-light guide spots in the initial tests, as our emphasis has been on fringe detection and analysis of the dispersed fringe. The optical path change as determined from the white light fringe is then compared to the optical path change determined from the HeNe fringe. Figure 2 shows the interferometer as seen from the light input side with the delay line in the background. Figure 3 shows the dispersing prism/mirror combination with the CCD camera behind it (behind the long wave pass filter).

3. TESTING OF INTERFEROMETER COMPONENTS

We tested certain performance criteria of the interferometer components before taking dispersed fringe data. Among these were:

- Characterization of the photo detector for the HeNe fringe monitoring, e.g. detector signal-to-noise, detector response as a function of spot position on the detector (misalignment of the beam depending on the DL position).
- Measure HeNe fringe visibility as a function of delay line position (tip-tilt dependent beam overlap etc).
- Measure DL secondary mirror PZT motion non-linearity.
- Calibrate HeNe fringe (PZT non-linearity, amplitude, visibility) and voltage range for linear part of HeNe fringe.
- Interferometer optical path stability.

The measured noise of the photo detector is by far not limiting the required measurement accuracy for the HeNe fringe, i.e. accuracy for the OPD measurement. Following are the results for some of the other measurements:

- Visibility vs. PZT motion: V drops by ~ 15% when moving the PZT by 4.5 μm (≡ 18 μm OPD). We changed the optical path usually by ~ 1.5 μm in the measurements.
- PZT non-linearity measurement for 4 μm PZT motion: factor ~ 2 when PZT is expanding, ~10% when contracting. ⇒ we took the data with the PZT's contracting.
- Interferometer stability measurements: 60 pm for 20 sec. averaging

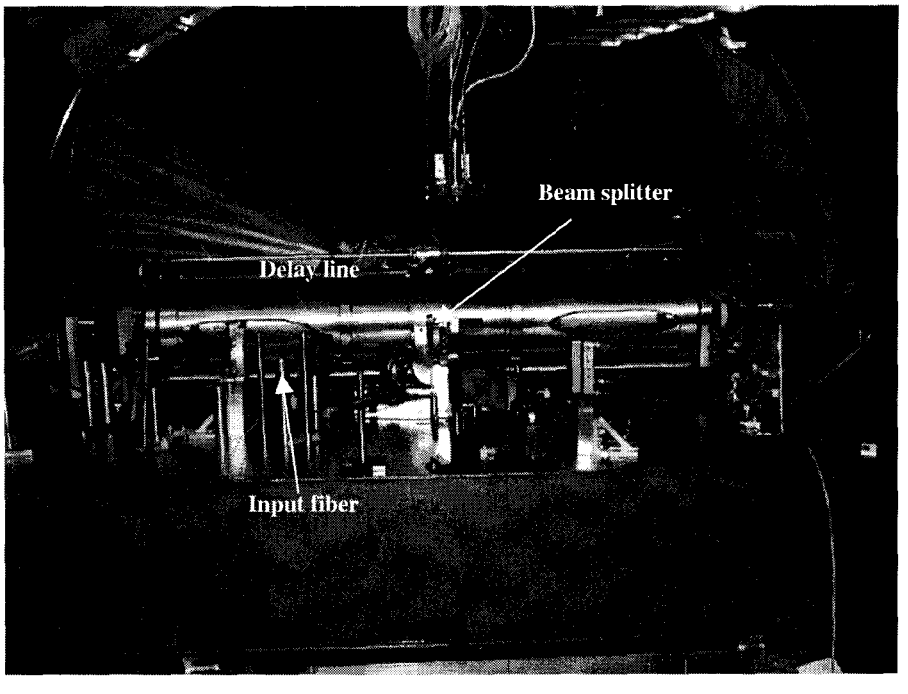

Figure 2 The interferometer inside the vacuum chamber with the beamsplitter in the center and the delay line in the background. In the background one can see the door of the vacuum chamber.

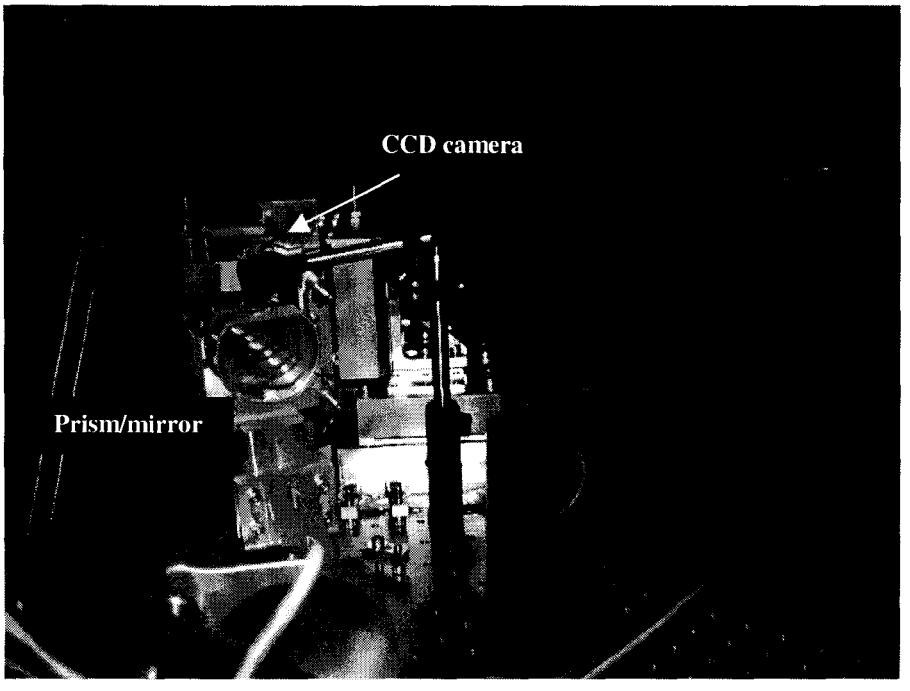

Figure 3 The dispersing element for the white light and the CCD camera. The light enter from the right through the stop, is dispersed by the prism before being focused onto the camera by the parabola (not seen, out of the plane in the foreground).

4. FRINGE DATA VS. OPTICAL PATH DIFFERENCE - EXPERIMENTS

All the experiments were conducted in still air; the vacuum chamber was tightly closed but not evacuated. However, it was floating on its air mounts (roll-off ~ 1Hz) to reduce any seismic noise and we usually waited about 2 hours after closing the doors for the inside temperature to stabilize. At the time of the experiments the interferometer beamsplitter could be adjusted remotely using picomotors to achieve maximum fringe visibility on the fringes. The delay line could be moved remotely as well using a DC motor to equalize the optical path for the two arms (0^{th} order fringe).

The data acquisition system and control of the delay line secondary mirrors is based on a real-time VME backplane running the VX-Works operating system.

The majority of the data were gathered using a DVC CCD camera with a frame rate of 30 Hz. The camera data were acquired with a Matrox 640 frame grabber VME board with the camera analog video signal as the input. During each frame acquisition the photo detectors were sampled at a 1 kHz rate and then averaged for 33.3 ms.

However, the SciMeasure CCD camera was installed in January 2000 and we have taken preliminary data using the analog output and the frame grabber module. We are currently modifying the data acquisition setup to incorporate the digital output of the SciMeasure CCD camera. The data will be discussed in section 5 as well.

The first series of experiments consisted of up to 50 sets of data with each set at a different initial optical path difference between the two arms (offsets, 10 – 100 nm/set). These data sets contained between 20 and 70 different optical path steps (dither steps). While the delay line PZT's were stepped through the offset and dither positions we acquired 1 to 10 CCD camera frames and saved a sub-image of 250 x 6 pixels at each position. Simultaneously we recorded the outputs of the three photo detectors for white light and HeNe power monitoring and the HeNe fringe intensity. Figure 4 shows the CCD intensity pattern for 70 dither steps as a function of wave number k (λ from ~710 to ~930 nm). This channel spectrum contains the information needed to determine the optical path changes. Figure 5 shows the projection of the channel spectra for offsets 1 - 5 across spectral channel 100. The optical path difference as determined from the data is than compared with the optical path difference determined from the HeNe fringe data. Figure 6 shows the HeNe fringe data that correspond to the white light data in figure 5. The data analysis and the results will be discussed in detail in section 5.

For the second series of experiments we moved only one delay line PZT for the dither steps. This was done to reduce a possible misalignment of the secondary mirrors as a result of the PZT motion. Due to the PZT hysteresis there still is a small offset between the different dither sets.

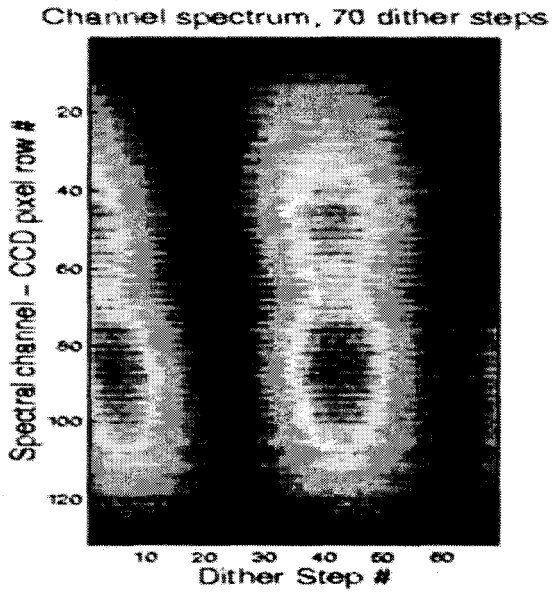

Figure 4 Dispersed fringe channel spectrum taken with the DVC camera. Shown is the fringe intensity vs. the dither steps for one offset from the 0^{th} order fringe. These data are averaged over 1 frame at each position.

The data analysis of the white light and HeNe fringes showed an amount of noise being present that needed to be reduced to achieve better results. We also observed that the alignment of the interferometer was not stable resulting in varying visibility and changes of arm lengths. The investigation of these effects revealed that:

- → the voltage applied to the delay line PZT's contained broadband noise and noise at 60 Hz and at ~50 kHz (is aliased down due to 1 kHz sampling rate), increasing the uncertainty in the HeNe fringe to 4 – 5 nm (the PZT response is ~ 4.5 μm/100 V with the optical path changing 4 times as much).
- → the beamsplitter did move on timescales of hours (temperature).
- → the delay line moved hundreds of microns (due to slow motion of the vacuum chamber).

We did suppress the noise on the PZT voltages substantially by adding 2-pole low-pass filtering (at 1 kHz) between the digital-to-analog converter (DAC) and the PZT high voltage supply. The optical path change uncertainty determined from the HeNe fringe data is now ≤ 1 nm. The beamsplitter mount was modified using PZT driven picomotors to allow remote tip-tilt adjustments. We now could align the beamsplitter without working inside the vacuum chamber and unavoidably heating the mount, the optical table and the air inside the chamber.

The delay line was locked down tightly while maintaining its position close to the 0^{th} order fringe. Unfortunately, this prevented any remote coarse motion (100 μm steps) of the delay line with the motor. However, the range of the second delay line PZT is more than enough to achieve equal arm length. The result was a very stable interferometer, which for days maintained almost the same optical path difference between the two arms.

It was also observed that the hysteresis of the delay line secondary mirror PZT/flexure mount changed from one data run to another. The preliminary conclusion is that there seems to be some stiction in the PZT/flexure assembly that is largest in the beginning of a data run (after the PZT had not been actuated for more than 15 minutes). We did not find the cause for the problem yet but for now we do go through 2 –3 complete dither cycles with the PZT before taking data. This does improve the quality of the data by avoiding unwanted changes of path length in the beginning of each data run.

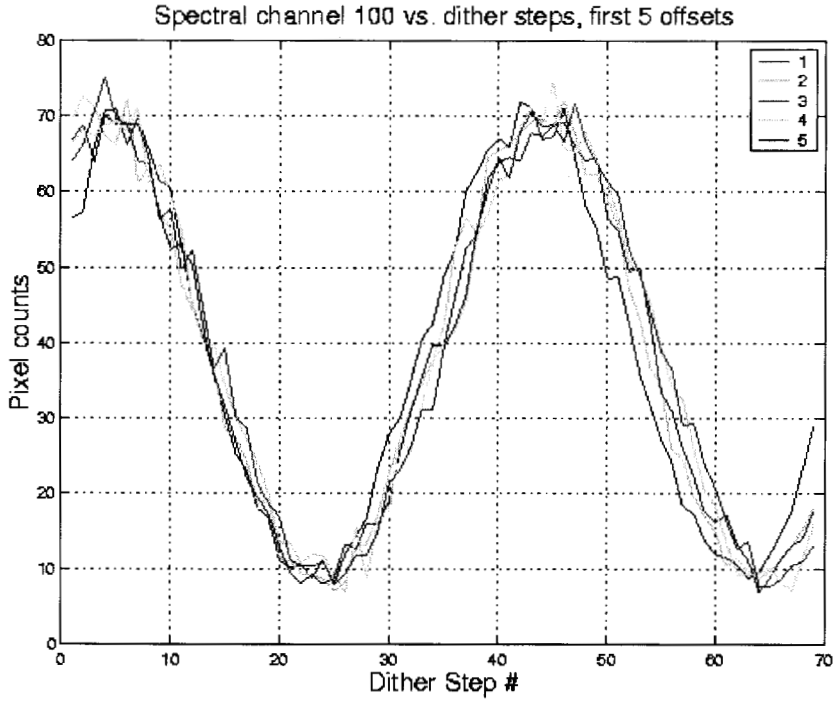

Figure 5 Plotted is spectral channel #100 of the channel spectrum (one wavenumber k) in figure 4 vs. the dither steps for the first five offsets from the 0^{th} order fringe.

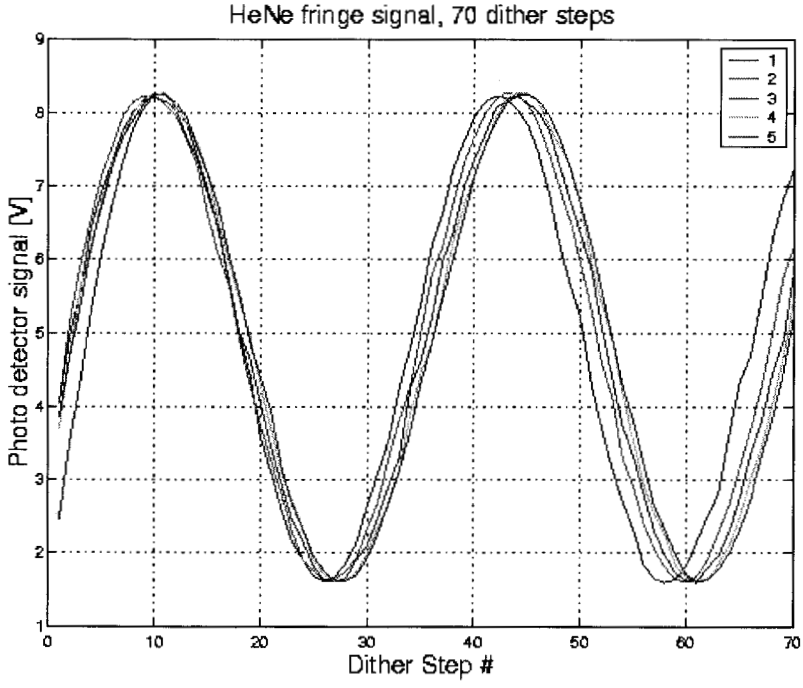

Figure 6 Plotted is the HeNe fringe vs. the dither steps for the first five offsets from the white light 0^{th} order fringe position.

5. WHITE LIGHT/HeNe FRINGE DATA ANALYSIS

In this section we describe our data analysis and the characterization of error sources in our experiments. The identified major error sources are detector noise and small unintended randomness in PZT dither positions. White light intensity drift and CCD bias drift are secondary error sources. We have not yet addressed the sensitivity to misalignments. However, in the current Michelson interferometer setup, the HeNe and white-light beams follow a common path. Thus we expect greatly reduced alignment sensitivity compared to the future non-common path implementation (section 6).

The goal of our experiments is to compare the optical path difference (OPD) between the two interferometer arms measured two ways. First, we measure the HeNe fringe on a single-pixel detector on one side of the beamsplitter. Secondly, we measure the dispersed white-light (700-900 nm) fringe using a row (or several summed rows) of a CCD on the other side of the beamsplitter. We perform this measurement for a range of initial OPDs, referred to as "offsets" in the ensuing discussion.

We modulate the optical path using the PZT-mounted secondary mirrors of the delay line. The optical path modulation allows us to fit sine waves, which are defined in Eq. (1), to the HeNe and to each CCD pixel (a 2-5 nm wide section of the white-light spectrum). Since each fit is an independent sine wave, we are insensitive to the pixel-to-pixel gain and offset differences. If the modulation is performed fast enough, we can also ignore temporal fluctuations in the gain and offset of each pixel, as well as in the HeNe detector. Typically a scan through 2 waves of the HeNe fringe takes 2 seconds.

Our signals are formed by stepping the mirror in 20-70 steps of ~ 20 nm (OPD). In the following discussion, each small step is called a "dither". The PZT dither has non-linear, hysteretic, and random components at the nanometer level. These effects will be accurately measured (and possibly removed with a closed-loop system) when the heterodyne metrology system is implemented[3]. However, with the present HeNe scheme, we have no ability to sense these effects at the peaks and valleys of the HeNe fringe. As described below, this places a noise floor of ~ 100 pm on our current experiments. It is worth noting that in SIM, a similar source of error occurs when the spacecraft rolls due to an imperfect attitude control system. The role will introduce many waves of optical path error for which there is no precise calibration. This will directly affect the ability to perform an accurate measurement of the guide interferometer beams and will have a smaller effect on the science interferometer (which uses attitude information fed from the guide interferometrs to calibrate external optical path differences).

Additionally, in both MAM and SIM, the precise CCD characteristics, alignment, and optical properties are not known *a priori* to the accuracy required performing picometer accuracy white-light fringe measurements. The important parameters (mean wavenumber per pixel, PZT step size, wavelength-dependent phase offset, etc.) must all be determined from the data. This is an integral part of the fringe detection process. Once these parameters are calibrated (fitted), a reduced set of parameters is fitted with the goal of determining the phase of the white-light fringe.

The fringe model we used in our algorithm at each offset, each wave number, and each dither position is given by

$$I_{ijl}^{data} = I_{jl}\{\,1+V_{jl}\cos(\,k_{jl}x_i+C_{jl}\,)\,\}, \qquad (1)$$

where l is the index for spectral channels, j is the index for offsets, i is the index for dither positions. For the HeNe l = 0. For the white light, l = 1,...n, which is the pixel index on CCD. $I_{jl}, V_{jl}, and\, C_{jl}$ are the fitted intensity, visibility, and phase offset, respectively, and all assumed to be constant over all dither positions x_i of given j,l. k_{jl} is the the wavenumber of the white light of j^{th} offset and l^{th} pixel on the CCD and is calculated with respect to the HeNe wavenumber k_{j0}. C_{jl} is the phase offset and consists of a geometric contribution and a non-geometric contribution. By "geometric" we refer to the linear phase delay vs. wavenumber whose slope is the OPD. The non-geometric part is related to optical properties of elements in our interferometer and is the same for all offsets. Our goal is to obtain phase delays in white light with less then 100 pm uncertainty relative to the HeNe phase delays from the dispersed white light fringe analysis repeated at many offsets. I_{ijl}^{data} is the normalized intensity at i^{th} dither position, j^{th} offset and l^{th} spectral channel. For white light, i.e. l = 1,...n, the normalized intensities are calculated from background-subtracted 8-bit digitized CCD image data and the white light power monitor detector. For the HeNe, i.e. l = 0, the fringe data points are normalized with respect to the intensity of the HeNe power monitor detector. The intensity monitors for the white light and the HeNe calibrate the fluctuations caused by the light sources and their coupling into the fiber. However, the fluctuations resulting from misalignments in the interferometer will still be present in the normalized intensity. Any fluctuation of the fitted parameters for a given offset will appear as residuals between the model and actual data, which will be discussed further in the actual data analysis.

To obtain an optimal phase delay estimate without prior calibration of either the effective wavenumbers or the non-geometric phase offsets, the interferometer is dithered with nearly equal step size over a range of ~ 1.5 μm starting at nearly

equal arm length, i.e. zero OPD. Offsetting near zero OPD minimizes the influence of an inaccuracy in effective white light wavenumbers extracted from the white light fringe analysis. The block diagram of the algorithm used is given in figure 7.

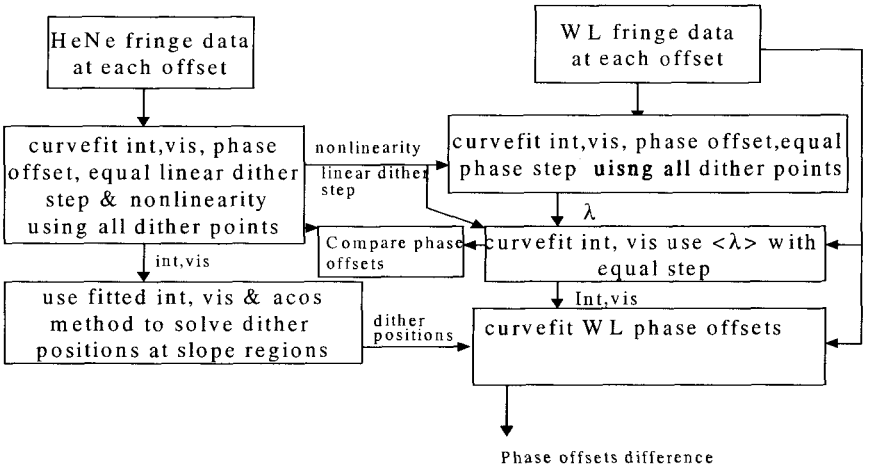

Figure 7 Block diagram of the white light/HeNe fringes analysis algorithm.

In the analysis, we started with the model of equal step size for the dither positions to extract the HeNe intensity, visibility, and phase offset. We then solved for the white light intensity, visibility, phase offset and used extracted dither positions of equal step size to solve for an effective wavenumber k_{jl} at each pixel on the CCD with respect to the HeNe wave number k_{j0}. In order to reduce the noise contribution from the fitted effective white light wavenumbers to our phase delay estimates, we used the mean effective wavenumbers $< k_{jl} >$, averaged over all measured offsets, to re-fit white light intensity, visibility and phase offset for each pixel on the CCD. For low detector noise cases, we can further improve the phase offset estimates of the dispersed white light fringes by using more accurate estimates of PZT positions derived from the HeNe data fits.

The white light delay estimate for each offset uses the phase delay rather than group delay, since the available spectral width of our white light source is narrow. The ratio of standard deviation between the group delay estimate and phase delay estimate is proportional to the ratio of mean wavenumber <k> over the usable bandwidth Δk of the white light[5]. We use the phase delay estimate in our analysis, since in our experiments $<k>/\Delta k$ is about 3.5. The implication of using phase delay over group delay is improved SNR with increased sensitivity to errors in the mean wavenumber.

The phase delays for the white light and HeNe data for November 5, 1999 1 frame data from the DVC CCD camera are plotted in figure 8. The standard deviation of the relative phase delays is 375 pm. We are able to consistently produce less than 500 pm standard deviations of relative phase delays between the white light and the HeNe using the commercial DVC CCD camera. Our first tests with the SciMeasure camera have further improved the standard deviation to be < 300 pm. The SciMeasure CCD camera in our initial non-digital "quick-and-dirty" implementation has a reduced noise level by a factor of 3.5 compared to DVC CCD camera. Also a better control of PZT positions has reduced the uncertainty from 4 nm level down to 1nm.

The root-mean-square (rms) residuals between the model and the November 5, 1999 data are plotted in figure 9. From the characteristics of residuals between model and data, we can identify the detector noise level and PZT position uncertainties. Quasi-periodic structures in the HeNe rms residuals are resulting from the 4 nm PZT position uncertainty with respect to the assumption of an equal dither step size. An additional constant shift of rms residuals in the white light with respect to the HeNe data stems from CCD noise. Drifts of white light intensity and/or CCD bias are observed to be < 0.5% in the fitted intensity and visibility from offset to offset. However, the signature of this noise is difficult to separate and quantify in the presence of detector and PZT motion noise.

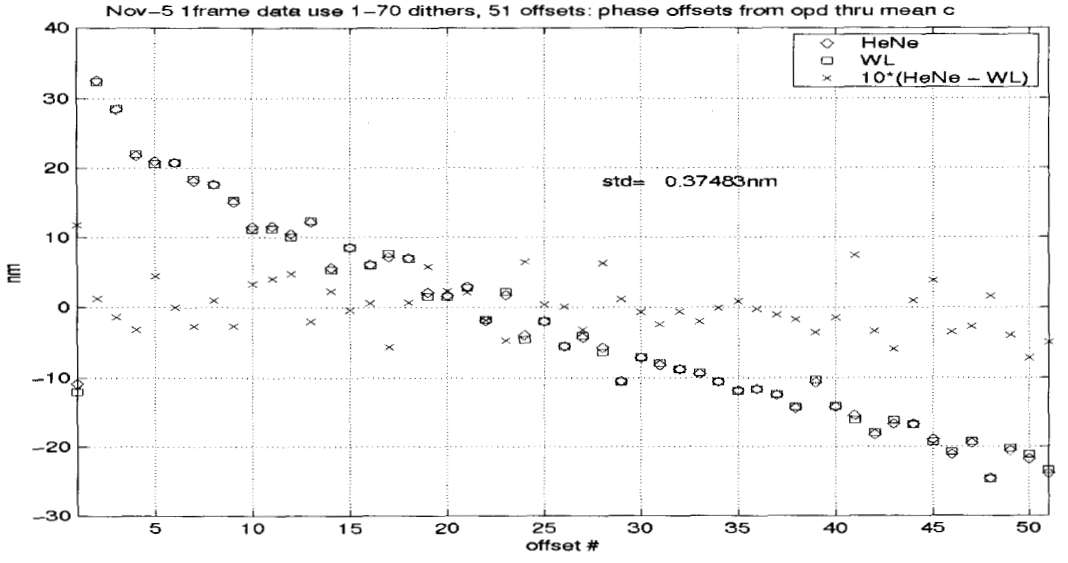

Figure 8 Phase delays of the white light/HeNe data taken on November 5,1999 1 frame data.

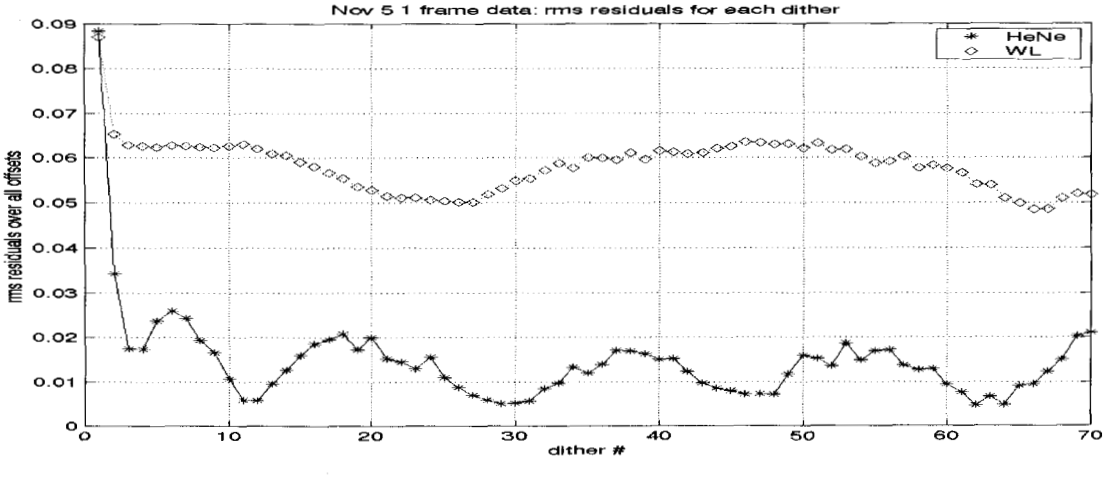

Figure 9 Residuals between model and the November 5, 1999 1-frame data vs. dither steps. Periodic structure results from 4 nm PZT uncertainty. The additional constant bias of rms residuals in the white light is from CCD noise.

A quantitative list of error sources in the November 5, 1999 data is given in Table 1. There is about 120 pm of error, which is not accounted for yet. The 186 pm of detector noise contribution is derived from synthesized white light fringes in the sole presence of detector noise, whose level is inferred from the standard deviation of fitting residuals from November 5 white light fringes. The unintended 4 nm PZT randomness is derived from the HeNe fringe analysis. The 300 pm contribution from the PZT uncertainty is obtained from synthesized white light fringes with a PZT uncertainty only with all corresponding parameters taken from the November 5 data. Intensity or bias drifts are estimated to be about 0.5%, which is deduced from the fitted intensity and visibility drifts from offset to offset.. We are not able to separate them unambiguously in the presence of high detector noise and PZT uncertainty. Again, the 37 pm or 49 pm of intensity drift or bias drift contribution is derived

from synthesized white light fringes. We calculated the total error contribution by taking the root-mean-square of the individual error sources. That is, we assume that all error sources are independent of each other.

Perturbation analysis result/total error	Magnitude	r.m.s. (W.L. - He-Ne) 375pm
Detector Noise	non-uniform spectrum Vis = 0.7425 mean SNR/pix = 17.07 n_pix=100, n_steps=70 lambda = 710-925 nm	186 pm
PZT Position	4 nm r.m.s. each dither pos'n	300 pm
Intensity Drift	0.5% over 1 offset	37pm
or Bias Drift	0.5% of mean Intensity over 1 offset	49pm
Unknown		**120pm**

Table 1 Error sources in the November 5, 1999 1 frame white light fringe data.

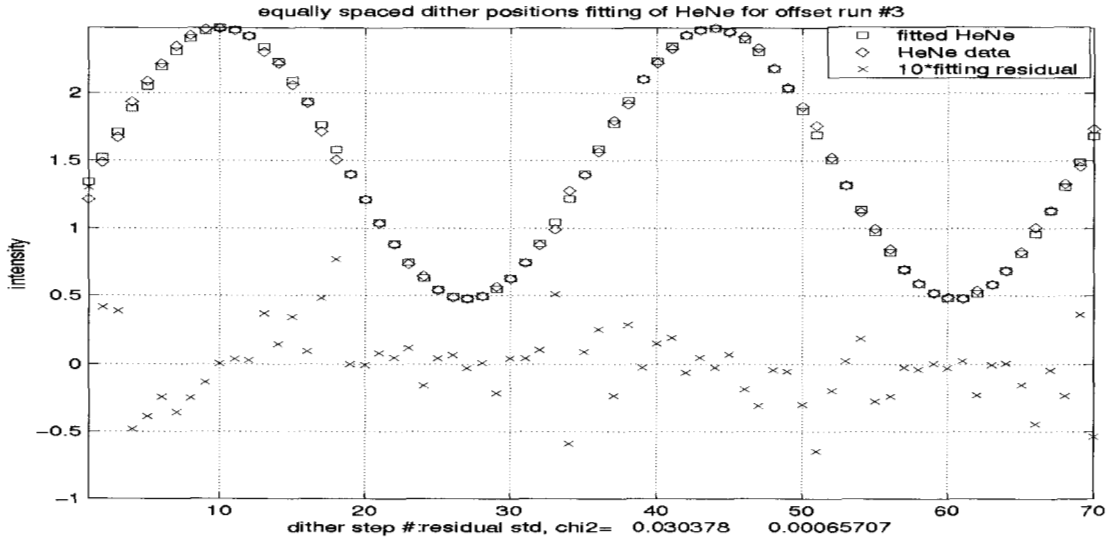

Figure 10 Model fitting of a HeNe fringe assuming equal dither step size for the PZT positions. Residuals are mostly contributed to by PZT position deviation from equal step size assumption.

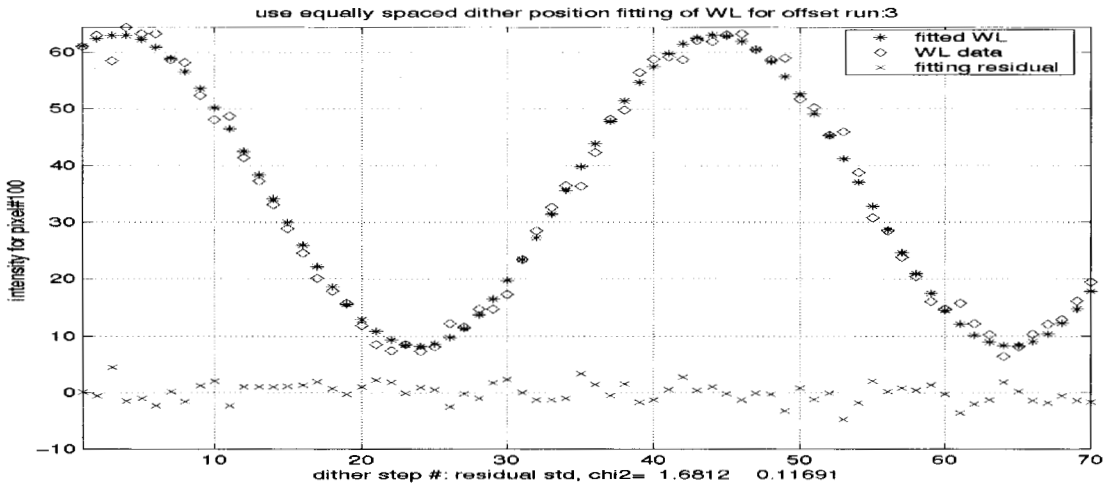

Figure 11 Model fitting of a white light fringe assuming an equal step size for the dither positions. Besides the PZT uncertainty contribution to rms residuals, CCD noise made a sizable contribution.

In figures 10 and 11 we show typical model fitting results to a HeNe and a white light fringe. The residuals in the HeNe are consistent with phase noise from the PZT uncertainty under equal dither step size assumption. The uncertainties are more visible in the linear slope regions. The amplitude noise in the stabilized HeNe fringes is negligibly small. The residuals in the white light are much larger compared to the HeNe residuals and are mostly from amplitude noise caused by the CCD with a small contribution from the PZT uncertainty. Residuals from CCD noise are more pronounced at the peaks and valleys of the white light fringe. This may be related to a non-linearity in the frame grabber, but this is still under investigation and may contribute partly to the unknown error source in table 1.

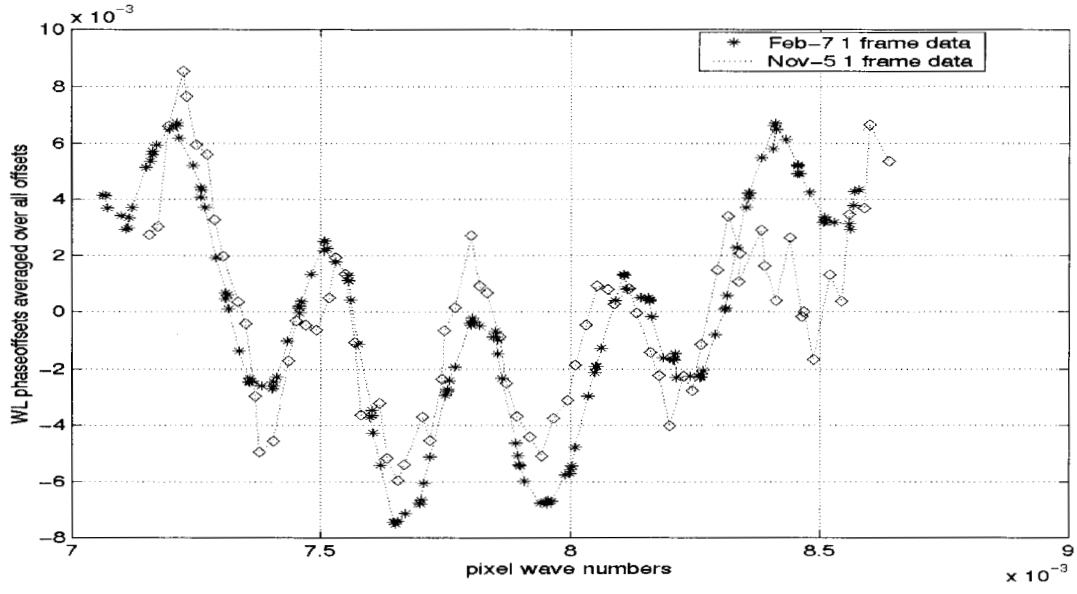

Figure 12 Non-geometric part of phase offsets in our interferometer extracted from thewhite light fringes of the November 5, 1999 1 frame data using the DVC CCD camera and the February 7, 2000 1 frame data using the SciMeasure CCD camera. Vertical-axis units are waves.

In figure 12, we plotted the estimated non-geometric part of the phase offsets from the white light fringe analysis. The non-geometric part of the phase offsets in our interferometers is fairly similar for two sets of data and consists of a quadratic and a periodic structure. The quadratic term is ~ 0.015 waves p-v, while the ringing is ~ 0.01 waves p-v. Since the interferometer is symmetric, we are not sure where the non-geometric phase originates from. It may be related to differences in the (nominally identical) optical coatings in each arm. Another possible source of the ringing is the non-symmetric sandwich beamsplitter. It has a glue layer on one side that is traversed twice by one beam and once by the other. The implication of the non-geometric phase is increased sensitivity to errors in the estimated wavenumber.

6. PHASE II – MODIFICATIONS TO THE INTERFEROMETER

The goal for the interferometer is to achieve agreement between the white light fringe analysis and the actual optical paths changes down to 20 pm. The accuracy of the actual paths change measurement will be improved by using the heterodyne interferometer metrology system that has been developed for MAM and ultimately for the SIM mission [3]. Figure 13 shows the modified interferometer configuration. Additionally, we will replace the interferometer beamsplitter with one that has a $\lambda/40$ figure.

In January 2000 we replaced the DVC CCD camera with a SciMeasure CCD camera [4]. This camera has much lower noise (5 e^-) and allows a higher frame read-out rate (up to 1 kHz full frame; 64 x 64 pixels). We are repeating the experiments using this camera now, the analysis of the new data is underway.

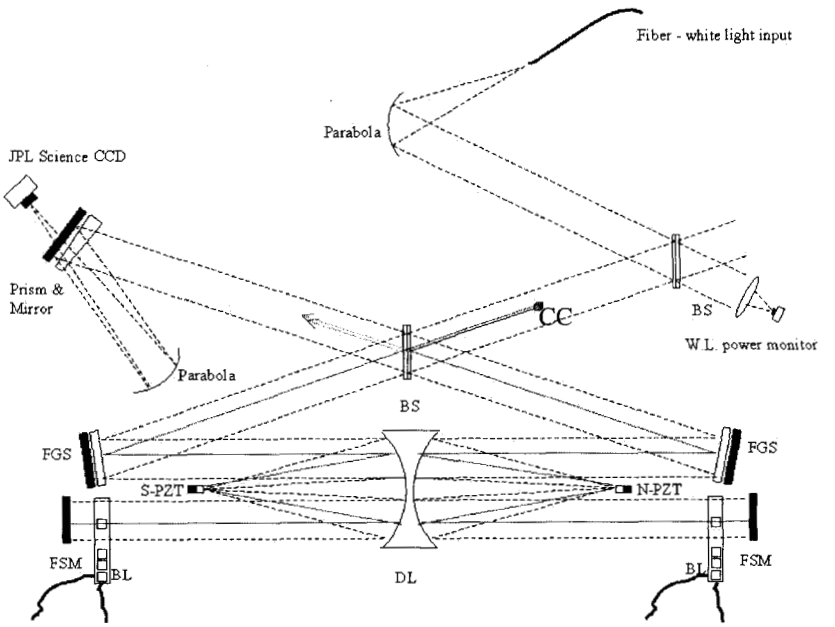

Figure 13 MAM interferometer in the phase II configuration. The length changes of the optical paths is measured with two heterodyne interferometers (BL – beamlaunchers). The internal arm paths are measured w.r.t. a common cube corner (CC). The CCD camera is the JPL developed science camera.

7. ACKNOWLEDGEMENTS

This research was carried out at the Jet Propulsion Laboratory, California Institute of Technology, under a contract with the National Aeronautics and Space Administration. We have received many helpful contributions from Roger Linfield and Dave van Buren.

8. REFERENCES

1. S.B. Shaklan et al, Micro-Arcsec Metrology Testbed (MAM), *Proceedings of SPIE Conf. on Astronomical Interferometry*, ed. Robert D. Reasenberg, Kona, Hawaii, March 20-24 1998, Vol. 3350, p. 1009.
2. S. Unwin et al, Science with the Space Interferometry Mission," *Proceedings of SPIE Conf. on Astronomical Interferometry*, ed. Robert D. Reasenberg , Kona, Hawaii, March 20-24 1998, Vol. 3350, p 551.
3. A. Kuhnert et al, Metrology system for the micro-arcsecond metrology testbed, *Proceedings of SPIE Conf. on Astronomical Interferometry*, ed. Robert D. Reasenberg , Kona, Hawaii, March 20-24 1998, Vol. 3350, p. 100
4. R. DuVarney et al, "EEV CCD39 wavefront sensors for ASO and interferometry", *SPIE International Symposium on Astronomical Telescopes and Instrumentation*, Munich, Germany, March 27 – 31, 2000.
5. R. Linfield, Statistical errors in group and phase delays, JPL internal memo.